

Electromagnetic Tomography of Radial Flow in the Quark-Gluon Plasma

Lipei Du^{1,2} and Ulrich Heinz³

¹*Department of Physics, University of California, Berkeley CA 94720*

²*Nuclear Science Division, Lawrence Berkeley National Laboratory, Berkeley CA 94720*

³*Department of Physics, The Ohio State University, Columbus, Ohio 43210*

(Dated: May 28, 2025)

We present a novel multimessenger approach to extract the effective radial flow of the quark-gluon plasma (QGP) by jointly analyzing thermal photon and dilepton spectra in heavy-ion collisions. A key feature of this method is that it circumvents the need for an unmeasurable reference—the temperature extracted from the photon spectrum in the absence of flow—by establishing a linear correlation between it and the dilepton-inferred temperature within a calibrated framework. By leveraging the complementary sensitivities of photons and dileptons, we define an effective radial flow observable that reflects early-time collectivity and expansion dynamics. We find that this observable exhibits a strong correlation with the spacetime-averaged radial velocity of the QGP, providing it with clear physical meaning as a measure of collective expansion. Together with previous results linking dilepton temperatures to initial QGP conditions, our work establishes a consistent framework for electromagnetic tomography of the QGP, offering direct access to its early-time dynamics.

INTRODUCTION

The quark-gluon plasma (QGP)—a deconfined state of quarks and gluons—is believed to have filled the early universe microseconds after the Big Bang [1, 2]. Today, relativistic heavy-ion collisions recreate this phase of matter under controlled laboratory conditions, enabling the study of its properties with increasing precision [3–5]. A hallmark of QGP evolution is its collective expansion, which is driven by pressure gradients and manifests in strong radial (transverse) flow. Understanding how this flow develops is crucial for revealing the medium’s Equation of State (EoS) and transport properties [6–8].

In cosmology, multimessenger astrophysics has emerged as a powerful paradigm [9]: combining gravitational waves and electromagnetic radiation from events such as neutron star mergers allows independent constraints on key physical quantities such as the Hubble constant [10]. Analogously, we here explore a multimessenger strategy in QGP tomography by jointly analyzing thermal photons (γ) and dileptons ($\ell\ell$)—electromagnetic probes that escape the medium with minimal final-state interactions [11–15]. These probes carry direct, time-dependent information about the evolving medium. However, unlike the Hubble flow in cosmology, the QGP’s expansion is anisotropic, rapidly evolving, and short-lived, making it significantly more challenging to characterize [16].

While both photons and dileptons are emitted throughout the QGP evolution, they exhibit different sensitivities to the medium’s conditions. Photons are blue-shifted due to the QGP’s transverse expansion, causing the temperature extracted from their spectra to appear higher than the actual thermal temperature [17–21]. Dilepton invariant mass spectra, in contrast, are comparatively insensitive to flow effects, offering a cleaner measure of the medium’s intrinsic temperature

[22–25]. Most thermal photons and dileptons are emitted earlier than hadrons, which undergo strong final-state interactions. This complementarity opens a unique opportunity: by contrasting photon and dilepton spectra, one can disentangle the effects of flow and temperature with tools that are intrinsically biased toward the most interesting early expansion stage—an enduring challenge in heavy-ion phenomenology.

The central difficulty in this approach lies in the inaccessibility of the baseline photon spectrum without flow. We show that this missing reference can be inferred through the dilepton-extracted temperature, exploiting a robust, nearly universal correlation observed in simulations calibrated by hadronic observables across different energies and centralities. This correlation enables the definition of an effective radial flow based solely on measurable electromagnetic signals, thus providing a novel, data-driven electromagnetic tomography of the dynamical evolution of the QGP.

FRAMEWORK AND SETUP

We simulate the spacetime evolution of heavy-ion collisions using a (3+1)-dimensional multistage hydrodynamic framework [26, 27]. The model comprises parametric initial conditions, the MUSIC hydrodynamics code [28, 29] for QGP evolution, the iS3D sampler [30] for particlization, and UrQMD [31, 32] for the hadronic afterburner. The hydrodynamic evolution solves the conservation equations for energy-momentum and net baryon number [26, 33, 34], incorporating viscous effects from shear stress and baryon diffusion while neglecting bulk viscosity [35]. The fluid is initialized at a fixed [36] proper time and evolved until particlization, which is defined on a freezeout surface of constant energy density [26, 27].

This modeling setup has been validated and its pa-

parameters calibrated through systematic comparison with hadronic observables [21, 23, 27, 37, 38]—including particle yields, transverse momentum spectra, and mean p_T of identified hadrons—both at midrapidity [39–41] and forward/backward rapidities [42–47], across nine beam energies from $\sqrt{s_{NN}} = 7.7$ to 200 GeV and eight centrality classes from 0–10% to 70–80%. This calibration ensures that the (3+1)-dimensional hydrodynamic evolution underlying the electromagnetic emission is physically realistic and consistent across beam energies, particularly in the evolution of temperature T , baryon chemical potential μ_B , and radial flow v_r , which directly affect the photon and dilepton spectra.

With the spacetime evolution in place, we compute thermal photon and dilepton spectra by integrating their emission rates over the full [48] hydrodynamic history [23, 49]. The local rest frame (LRF) emission rates are computed using thermal field theory [50] via the electromagnetic spectral function $\text{Im} \Pi_{\text{em}}(k; T, \mu_B)$, derived from the retarded photon self-energy $\Pi_{\text{em}}^{\mu\nu}$ incorporating QCD corrections. In the LRF of each fluid cell with (T, μ_B) , we evaluate the photon rate $\omega d^3\Gamma_\gamma/d^3\mathbf{k}$ [51, 52] and dilepton rate $d^4\Gamma_{\ell\bar{\ell}}/d\omega d^3\mathbf{k}$ [23, 53, 54], both of which include complete $O(\alpha_s)$ contributions as well as Landau-Pomeranchuk-Migdal effects. The four-momentum $k^\mu = (\omega, \mathbf{k})$ satisfies $M = \sqrt{\omega^2 - |\mathbf{k}|^2}$, with invariant mass $M=0$ for photons and $M>0$ for dileptons. These rates are then boosted to the laboratory frame using the local four-velocity $u^\mu(x)$ of the fluid. We include the dependence on μ_B in the rates [23, 52], but neglect viscous corrections to ensure consistency between photon and dilepton treatments, since the viscous corrections to dilepton rates remain under development. To isolate thermal QGP radiation [21, 24], only fluid cells with temperatures above the Cleymans freezeout line [40, 55] are considered.

After boosting and integrating over spacetime and phase-space variables [23, 49], we obtain the dilepton invariant mass spectra $dN_{\ell\bar{\ell}}/(dM dy)$ and photon transverse momentum spectra $dN_\gamma/(2\pi p_T dp_T dy)$. These results have been benchmarked [21, 23, 24] against experimental data from the STAR [56–59] and PHENIX [60–62] Collaborations, validating the framework’s ability to describe electromagnetic observables. To extract “effective temperatures”, we fit the photon p_T spectra at midrapidity within the range $p_T \in [0.8, 2]$ GeV to an exponential form $dN_\gamma/(p_T dp_T) \propto \exp(-p_T/T_\gamma)$ [18, 20, 63]. Similarly, the dilepton spectra at midrapidity are fitted to the parametrization $dN_{\ell\bar{\ell}}/dM \propto (M T_{\ell\bar{\ell}})^{3/2} \exp(-M/T_{\ell\bar{\ell}})$ for $M \in [1, 3]$ GeV [22–24]. These extracted “temperatures”, T_γ and $T_{\ell\bar{\ell}}$, provide measures of the effective thermal scale probed by each observable.

To determine the effective radial flow, we compute photon temperatures with and without [64] transverse expansion, denoted as T_γ and $T_{\gamma 0}$, respectively. The difference between them reflects the Doppler blue shift induced by

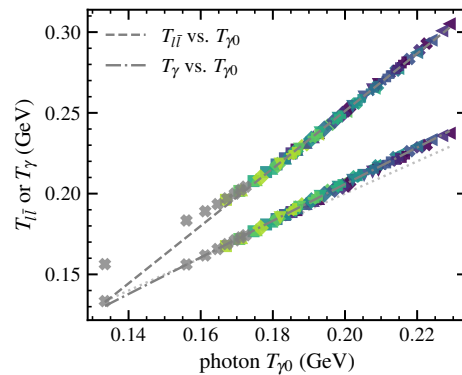


Figure 1. Temperatures at midrapidity extracted from dilepton invariant mass spectra ($T_{\ell\bar{\ell}}$, upper line) and photon transverse momentum spectra (T_γ , lower line), plotted against the photon temperature extracted from spectra without transverse flow ($T_{\gamma 0}$) (see the Supplemental Material for a table containing all data points; same for Fig. 2). Linear fits are shown for each set, excluding the gray points corresponding to $\sqrt{s_{NN}} = 7.7$ GeV. The dotted line indicates $y = x$.

radial flow. We extract the effective radial flow velocity v_r^{eff} using the relativistic blue-shift relation:

$$T_\gamma = T_{\gamma 0} \sqrt{(1 + v_r^{\text{eff}})/(1 - v_r^{\text{eff}})}. \quad (1)$$

RESULTS

Extraction of effective temperatures from electromagnetic spectra

Figure 1 compares temperatures extracted from dilepton ($T_{\ell\bar{\ell}}$) and photon (T_γ) spectra with those obtained from photon spectra in the absence of transverse expansion ($T_{\gamma 0}$). We begin by examining the photon temperatures with and without flow, indicated by the lower set of markers. As expected, T_γ is systematically higher than $T_{\gamma 0}$, reflecting the Doppler blue-shift from radial expansion. The difference diminishes at lower beam energies, consistent with a less-developed transverse flow in cooler, shorter-lived fireballs. At the lowest energy, $\sqrt{s_{NN}} = 7.7$ GeV, T_γ and $T_{\gamma 0}$ nearly coincide, indicating minimal blue shift experienced by the photon spectra.

This systematic shift between T_γ and $T_{\gamma 0}$ offers a practical route to disentangle flow and temperature effects using Eq. (1). However, because $T_{\gamma 0}$ is experimentally inaccessible, an alternative baseline is needed. Motivated by the flow-insensitivity of dilepton invariant mass spectra [13, 22], we explore the correlation between $T_{\ell\bar{\ell}}$ and $T_{\gamma 0}$. Earlier work of one of the authors has shown that, at $\sqrt{s_{NN}} = 7.7$ and 14.5 GeV, the time-dependent $T_{\ell\bar{\ell}}$ and $T_{\gamma 0}$ differ by an approximately constant offset ($\Delta T \equiv T_{\ell\bar{\ell}} - T_{\gamma 0}$) throughout the evolution [21]. In the Supplemental Material, we expand this observation and

demonstrate that the offset holds across a broad range of energies and centralities, although the time-resolved nature of this correlation limits its direct experimental applicability.

We next examine the correlation between $T_{\ell\bar{\ell}}$ and $T_{\gamma 0}$ extracted from fully spacetime-integrated spectra. A strong linear trend is observed, indicated by the upper line of markers in Fig. 1, with deviations only at the lowest beam energies and peripheral collisions (see footnotes [36, 48]). Interestingly, the integrated $T_{\ell\bar{\ell}}$ increasingly exceeds $T_{\gamma 0}$ at higher beam energies, a natural consequence of the longer fireball lifetime, which accentuates the offset ΔT accumulated over time. Furthermore, $T_{\ell\bar{\ell}}$ exhibits a steeper slope than T_{γ} when plotted against $T_{\gamma 0}$. This reflects the stronger temperature sensitivity of dilepton emission rates [23, 65] compared to those of photons [63, 66]: dileptons are preferentially emitted from hotter regions, which skews the extracted temperature upward relative to $T_{\gamma 0}$ and the blue-shifted T_{γ} .

Crucially, the robust correlation between $T_{\ell\bar{\ell}}$ and $T_{\gamma 0}$ allows experimental estimation of the otherwise unmeasurable $T_{\gamma 0}$ using dilepton data. Quantitatively, a global linear fit to the data (excluding $\sqrt{s_{NN}} = 7.7$ GeV) gives

$$T_{\ell\bar{\ell}} = (1.78 \pm 0.01) T_{\gamma 0} - (10.5 \pm 0.2) \times 10^{-2} \text{ GeV}, \quad (2)$$

allowing $T_{\gamma 0}$ to be inferred from $T_{\ell\bar{\ell}}$ for use in Eq. (1). This forms the core of our data-driven strategy to extract radial flow from electromagnetic probes. Dileptons act as baseline thermometers, while photons serve as flow-sensitive blue-shift meters—together enabling the separation of temperature and flow effects that are otherwise entangled in observed spectra.

Physical interpretation of the effective radial flow

To evaluate the physical meaning of the extracted flow observable v_r^{eff} from Eq. (1), we compare it with flow quantities obtained directly from the underlying multi-stage hydrodynamic model calibrated by hadronic observables. Identifying such correlations is generally beyond experimental reach and only accessible through realistic modeling. Figure 2 presents this comparison, showing v_r^{eff} alongside two reference quantities: v_r^{prefrz} , computed from fluid cells with temperatures above the freezeout line over the entire evolution, and v_r^{frz} , calculated from fluid cells on the freezeout surface. Both quantities are defined as weighted averages of u^r/u^t using $e\gamma$ as the weight, where e is the local energy density and $\gamma = u^t$ is the Lorentz boost factor. A strong correlation emerges between v_r^{eff} and v_r^{prefrz} , while no such trend is observed with v_r^{frz} .

Focusing first on the scatter of v_r^{frz} versus v_r^{eff} , the absence of a universal correlation indicates that v_r^{eff} is not simply a reflection of final-state properties near

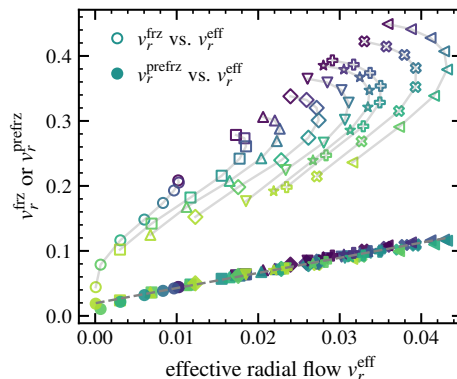


Figure 2. Comparison between the effective radial flow v_r^{eff} extracted from electromagnetic spectra and hydrodynamic flow benchmarks: v_r^{prefrz} (lower line), the spacetime-averaged radial velocity of fluid cells above the freezeout surface, and v_r^{frz} (upper cloud), the averaged flow velocity on the freezeout surface. Points at fixed beam energy but varying centrality are connected by gray lines to guide the eye. A linear fit to v_r^{prefrz} versus v_r^{eff} is also shown.

hadronization, as captured by v_r^{frz} . Interestingly, the centrality dependence of these two flow observables also differs at fixed beam energy, as illustrated by gray lines connecting points across centralities. Moving from central to peripheral collisions (top to bottom along each line), v_r^{frz} (vertical axis) decreases monotonically, consistent with reduced final-state flow in smaller systems. By contrast, v_r^{eff} (horizontal axis) increases from central to mid-central collisions, then decreases—revealing a non-monotonic trend.

This behavior is notable: the centrality dependence of v_r^{frz} aligns with that of the mean p_T of final hadrons [40, 41], both reflecting the stronger flow built up in hotter, longer-lived fireballs formed in central collisions. However, the centrality trend of v_r^{eff} more closely resembles that of hadronic v_2 , which peaks at intermediate centralities [67, 68]. This is consistent with v_r^{eff} being sensitive to the early-time development of transverse flow along the short axis of the almond-shaped initial geometry [16]—a feature captured by electromagnetic emission at early times. That final hadron v_2 exhibits a similar trend is not surprising, as it reflects the final anisotropic flow developed throughout the evolution, but rooted in the same initial geometry. In this light, it would be valuable to experimentally measure the mean p_T of photons across centralities: such measurements are expected to exhibit a similar non-monotonic trend.

The strong correlation between v_r^{eff} and v_r^{prefrz} lends this observable clear physical significance. By definition, v_r^{prefrz} is the energy-density-weighted radial flow of all fluid cells above the freezeout line, integrated over the entire QGP evolution. That v_r^{eff} tracks this quantity so closely confirms its role as a spacetime-integrated measure of collective expansion, preceding hadronization.

This is expected: electromagnetic probes are continuously emitted throughout the QGP evolution, with a natural bias toward early times when temperatures—and thus emission rates—are highest. In this context, we interpret v_r^{eff} as a temperature-weighted, early-time-sensitive radial flow observable. Crucially, this electromagnetic “flowmeter” complements hadronic observables that are more sensitive to the late stages, providing a rare experimental window into the development of collectivity when the QGP is still hot and dense.

Time sensitivity of flow observables and complementarity

To further illustrate the complementarity between electromagnetic and hadronic flow observables, Figure 3 compares four distinct radial flow quantities at $\sqrt{s_{\text{NN}}} = 19.6$ and 200 GeV: the effective radial flow v_r^{eff} extracted from electromagnetic probes, the spacetime-averaged pre-freezeout flow v_r^{prefrz} , the average freezeout surface flow v_r^{frz} , and the kinetic freezeout velocity v_r^{kin} obtained from blast-wave [69] fits to hadronic spectra [40]. Over the range shown here all four flow measures increase with beam energy, reflecting the stronger pressure gradients and more explosive expansion of hotter and longer-lived fireballs at higher energies.

A clear hierarchy is observed among the flow quantities at a fixed collision energy:

$$v_r^{\text{eff}} < v_r^{\text{prefrz}} < v_r^{\text{frz}} < v_r^{\text{kin}}. \quad (3)$$

This ordering reflects the layered temporal structure of QGP expansion and emission. Photons and dileptons are emitted predominantly at early times, when the temperature is high but the flow is still modest, allowing them to probe the onset of collectivity. The hydrodynamic average v_r^{prefrz} records the full spacetime development of flow, but remains biased toward early stages due to the temperature dependence of energy weighting. Here, we note that although both are spacetime-averaged over the entire evolution, v_r^{eff} is consistently smaller than v_r^{prefrz} in magnitude. This difference arises because electromagnetic emission is more heavily weighted toward the hottest regions (i.e. with a higher power of T [70]) than the energy density weightings used in defining v_r^{prefrz} . In contrast, hadronic observables capture the final-state expansion: v_r^{frz} reflects conditions at chemical freezeout, while v_r^{kin} additionally accounts for hadronic acceleration between chemical and kinetic freezeout [71, 72].

Figure 3 thus encapsulates the continuous development of radial flow, with each observable providing sensitivity to a different stage of the system’s evolution. It highlights the importance of electromagnetic probes in accessing early-time dynamics that are inaccessible to hadronic measurements. As a potential application, recalling the strong dependence of the early-time expansion on the

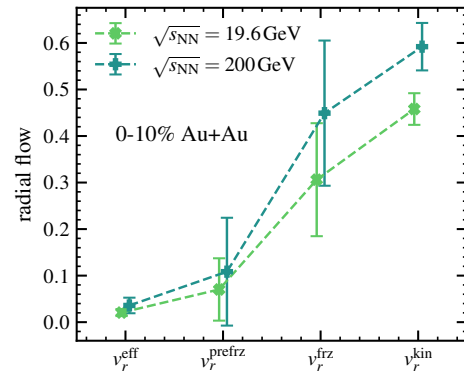


Figure 3. Radial flow observables at $\sqrt{s_{\text{NN}}} = 19.6$ and 200 GeV: the effective flow v_r^{eff} extracted from electromagnetic spectra, the pre-freezeout average v_r^{prefrz} from hydrodynamics, the freezeout surface average v_r^{frz} , and the kinetic freezeout velocity v_r^{kin} obtained from blast-wave fits to hadronic spectra. The error bars for v_r^{eff} and v_r^{kin} reflect fitting uncertainties, while those for v_r^{prefrz} and v_r^{frz} represent the variations among fluid cells contributing to the corresponding averages.

EoS at the highest temperatures, the extracted v_r^{eff} offers a promising new avenue for constraining the EoS from electromagnetic observables. Although v_r^{eff} is numerically small, its significance lies in its temperature-weighted spacetime-averaged nature—it integrates over the entire expansion history, but with a bias toward the early, hottest stages. Combined with hadronic flow observables, which capture the final outcome of this evolution, the two jointly offer a more complete picture of QGP dynamics. By breaking through the limitations of analyses based entirely on hadronic observables, this multimessenger approach can help to establish a more differential and time-resolved picture of QGP collectivity in heavy-ion collisions.

SUMMARY

We have introduced a novel multimessenger framework for extracting the effective radial flow of the QGP before its decay into hadrons by combining thermal photon and dilepton measurements in relativistic heavy-ion collisions. This approach exploits the distinct sensitivities of the two probes—dilepton invariant mass spectra serve as a clean thermometer unaffected by collective motion, while photon transverse momentum spectra are blue-shifted by flow, acting as a dynamical flowmeter.

A central feature of the method is its circumvention of the unobservable no-flow photon baseline. By establishing a robust, model-calibrated correlation between dilepton-inferred temperatures and the no-flow photon temperature baseline, we reconstruct the spectral blue-shift attributable to transverse expansion. The resulting effective flow observable is significantly smaller

in magnitude than final-state hadronic flow, consistent with the early-time dominance of electromagnetic emission. Nonetheless, it shows a strong correlation with the spacetime-averaged radial velocity of the medium prior to freezeout, giving it a physically meaningful interpretation as a time-integrated measure of QGP expansion dynamics.

Together with earlier findings that relate dilepton temperatures to the initial QGP temperatures [24], this work completes a comprehensive framework in which electromagnetic probes map both the thermal and dynamical evolution of the fireball: dileptons function as thermometers for the early state, and the photon-dilepton comparison yields a flowmeter for early-time collectivity. This enables a new form of electromagnetic tomography that captures the early-time structure of QGP expansion, complementing hadronic observables that are sensitive to later stages.

Applied to current and upcoming datasets at RHIC and the LHC, this method enhances the utility of electromagnetic radiation as a precision tool for QGP studies, opening the door to applications in small systems such as high-multiplicity p - p or p -A collisions, where the nature of collectivity remains under active investigation. It also lays the groundwork for future studies aimed at further resolving the time evolution of flow through even more differential analyses of the photon transverse momentum and dilepton mass spectra, eventually establishing electromagnetic tomography as a prime tool for precision studies of early-time flow and collectivity in hot and dense QCD matter.

ACKNOWLEDGEMENTS

L.D. [73] acknowledges useful conversations with Shuzhe Shi. This work was supported in part by the U.S. Department of Energy (DOE), Office of Science, Office of Nuclear Physics, under DOE Award No. DE-SC0004286 (U.H.). Computations were made on the computers managed by the Ohio Supercomputer Center [74].

-
- [1] P. Braun-Munzinger and J. Wambach, “The Phase Diagram of Strongly-Interacting Matter,” *Rev. Mod. Phys.* **81**, 1031–1050 (2009), [arXiv:0801.4256 \[hep-ph\]](#).
 - [2] Edward Shuryak, “Strongly coupled quark-gluon plasma in heavy ion collisions,” *Rev. Mod. Phys.* **89**, 035001 (2017), [arXiv:1412.8393 \[hep-ph\]](#).
 - [3] Berndt Muller, Jurgen Schukraft, and Boleslaw Wyslouch, “First Results from Pb+Pb collisions at the LHC,” *Ann. Rev. Nucl. Part. Sci.* **62**, 361–386 (2012), [arXiv:1202.3233 \[hep-ex\]](#).
 - [4] Adam Bzdak, Shinichi Esumi, Volker Koch, Jinfeng Liao, Mikhail Stephanov, and Nu Xu, “Mapping the Phases of Quantum Chromodynamics with Beam Energy Scan,” *Phys. Rept.* **853**, 1–87 (2020), [arXiv:1906.00936 \[nucl-th\]](#).
 - [5] Lipei Du, Agnieszka Sorensen, and Mikhail Stephanov, “The QCD phase diagram and Beam Energy Scan physics: A theory overview,” *Int. J. Mod. Phys. E* **33**, 2430008 (2024), [arXiv:2402.10183 \[nucl-th\]](#).
 - [6] Jonah E. Bernhard, J. Scott Moreland, and Steffen A. Bass, “Bayesian estimation of the specific shear and bulk viscosity of quark–gluon plasma,” *Nature Phys.* **15**, 1113–1117 (2019).
 - [7] D. Everett *et al.* (JETSCAPE), “Phenomenological constraints on the transport properties of QCD matter with data-driven model averaging,” *Phys. Rev. Lett.* **126**, 242301 (2021), [arXiv:2010.03928 \[hep-ph\]](#).
 - [8] Govert Nijs, Wilke van der Schee, Umut Gürsoy, and Raimond Snellings, “Transverse Momentum Differential Global Analysis of Heavy-Ion Collisions,” *Phys. Rev. Lett.* **126**, 202301 (2021), [arXiv:2010.15130 \[nucl-th\]](#).
 - [9] Péter Mészáros, Derek B. Fox, Chad Hanna, and Kohta Murase, “Multi-Messenger Astrophysics,” *Nature Rev. Phys.* **1**, 585–599 (2019), [arXiv:1906.10212 \[astro-ph.HE\]](#).
 - [10] Tim Dietrich, Michael W. Coughlin, Peter T. H. Pang, Mattia Bulla, Jack Heinzl, Lina Issa, Ingo Tews, and Sarah Antier, “Multimessenger constraints on the neutron-star equation of state and the Hubble constant,” *Science* **370**, 1450–1453 (2020), [arXiv:2002.11355 \[astro-ph.HE\]](#).
 - [11] Edward V. Shuryak, “Quark-Gluon Plasma and Hadronic Production of Leptons, Photons and Psions,” *Phys. Lett. B* **78**, 150 (1978).
 - [12] K. Kajantie and H. I. Miettinen, “Temperature Measurement of Quark-Gluon Plasma Formed in High-Energy Nucleus-Nucleus Collisions,” *Z. Phys. C* **9**, 341 (1981).
 - [13] Larry D. McLerran and T. Toimela, “Photon and Dilepton Emission from the Quark - Gluon Plasma: Some General Considerations,” *Phys. Rev. D* **31**, 545 (1985).
 - [14] R. C. Hwa and K. Kajantie, “Diagnosing Quark Matter by Measuring the Total Entropy and the Photon Or Dilepton Emission Rates,” *Phys. Rev. D* **32**, 1109 (1985).
 - [15] K. Kajantie, Joseph I. Kapusta, Larry D. McLerran, and A. Mekjian, “Dilepton Emission and the QCD Phase Transition in Ultrarelativistic Nuclear Collisions,” *Phys. Rev. D* **34**, 2746 (1986).
 - [16] Ulrich Heinz and Raimond Snellings, “Collective flow and viscosity in relativistic heavy-ion collisions,” *Ann. Rev. Nucl. Part. Sci.* **63**, 123–151 (2013), [arXiv:1301.2826 \[nucl-th\]](#).
 - [17] Hendrik van Hees, Charles Gale, and Ralf Rapp, “Thermal Photons and Collective Flow at the Relativistic Heavy-Ion Collider,” *Phys. Rev. C* **84**, 054906 (2011), [arXiv:1108.2131 \[hep-ph\]](#).
 - [18] Chun Shen, Ulrich W Heinz, Jean-Francois Paquet, and Charles Gale, “Thermal photons as a quark-gluon plasma thermometer reexamined,” *Phys. Rev. C* **89**, 044910 (2014), [arXiv:1308.2440 \[nucl-th\]](#).
 - [19] Jean-François Paquet, Chun Shen, Gabriel S. Denicol, Matthew Luzum, Björn Schenke, Sangyong Jeon, and Charles Gale, “Production of photons in relativistic heavy-ion collisions,” *Phys. Rev. C* **93**, 044906 (2016), [arXiv:1509.06738 \[hep-ph\]](#).
 - [20] Jean-François Paquet, “Thermal photon production in Gubser inviscid relativistic fluid dynamics,” *Phys. Rev. C* **108**, 064912 (2023), [arXiv:2305.10669 \[nucl-th\]](#).

- [21] Lipei Du, “Multimessenger study of baryon-charged QCD matter in heavy-ion collisions,” *Phys. Lett. B* **861**, 139270 (2025), [arXiv:2408.08501 \[nucl-th\]](#).
- [22] Ralf Rapp and Hendrik van Hees, “Thermal Dileptons as Fireball Thermometer and Chronometer,” *Phys. Lett. B* **753**, 586–590 (2016), [arXiv:1411.4612 \[hep-ph\]](#).
- [23] Jessica Churchill, Lipei Du, Charles Gale, Greg Jackson, and Sangyong Jeon, “Dilepton production at next-to-leading order and intermediate invariant-mass observables,” *Phys. Rev. C* **109**, 044915 (2024), [arXiv:2311.06675 \[nucl-th\]](#).
- [24] Jessica Churchill, Lipei Du, Charles Gale, Greg Jackson, and Sangyong Jeon, “Virtual Photons Shed Light on the Early Temperature of Dense QCD Matter,” *Phys. Rev. Lett.* **132**, 172301 (2024), [arXiv:2311.06951 \[nucl-th\]](#).
- [25] Olaf Massen, Govert Nijs, Mike Sas, Wilke van der Schee, and Raimond Snellings, “Effective temperatures of the QGP from thermal photon and dilepton production,” *Eur. Phys. J. C* **85**, 388 (2025), [arXiv:2412.09671 \[nucl-th\]](#).
- [26] Chun Shen and Sahr Alzhrani, “Collision-geometry-based 3D initial condition for relativistic heavy-ion collisions,” *Phys. Rev. C* **102**, 014909 (2020), [arXiv:2003.05852 \[nucl-th\]](#).
- [27] Lipei Du, Han Gao, Sangyong Jeon, and Charles Gale, “Rapidity scan with multistage hydrodynamic and statistical thermal models,” *Phys. Rev. C* **109**, 014907 (2024), [arXiv:2302.13852 \[nucl-th\]](#).
- [28] Bjoern Schenke, Sangyong Jeon, and Charles Gale, “(3+1)D hydrodynamic simulation of relativistic heavy-ion collisions,” *Phys. Rev. C* **82**, 014903 (2010), [arXiv:1004.1408 \[hep-ph\]](#).
- [29] Bjorn Schenke, Sangyong Jeon, and Charles Gale, “Elliptic and triangular flow in event-by-event (3+1)D viscous hydrodynamics,” *Phys. Rev. Lett.* **106**, 042301 (2011), [arXiv:1009.3244 \[hep-ph\]](#).
- [30] Mike McNelis, Derek Everett, and Ulrich Heinz, “Particleization in fluid dynamical simulations of heavy-ion collisions: The iS3D module,” *Comput. Phys. Commun.* **258**, 107604 (2021), [arXiv:1912.08271 \[nucl-th\]](#).
- [31] S. A. Bass *et al.*, “Microscopic models for ultrarelativistic heavy ion collisions,” *Prog. Part. Nucl. Phys.* **41**, 255–369 (1998), [arXiv:nucl-th/9803035](#).
- [32] M. Bleicher *et al.*, “Relativistic hadron hadron collisions in the ultrarelativistic quantum molecular dynamics model,” *J. Phys. G* **25**, 1859–1896 (1999), [arXiv:hep-ph/9909407](#).
- [33] Gabriel S. Denicol, Charles Gale, Sangyong Jeon, Akihiko Monnai, Björn Schenke, and Chun Shen, “Net baryon diffusion in fluid dynamic simulations of relativistic heavy-ion collisions,” *Phys. Rev. C* **98**, 034916 (2018), [arXiv:1804.10557 \[nucl-th\]](#).
- [34] Lipei Du and Ulrich Heinz, “(3+1)-dimensional dissipative relativistic fluid dynamics at non-zero net baryon density,” *Comput. Phys. Commun.* **251**, 107090 (2020), [arXiv:1906.11181 \[nucl-th\]](#).
- [35] Despite some recent studies (e.g. [75, 76]) bulk viscosity remains largely unconstrained at finite baryon chemical potential, and hence a systematic investigation of its influence on electromagnetic probes is left for future work.
- [36] Reflecting the longer prehydrodynamic phase associated with the extended nuclear interpenetration time, initialization time τ_0 increases with decreasing center-of-mass energy. We have verified that the correlation presented in Fig. 1 is robust under variations in τ_0 . Specifically, for $\sqrt{s_{NN}} = 7.7$ GeV, decreasing τ_0 (i.e. assuming earlier hydrodynamization) shifts the markers in Fig. 1 upward and to the right; they remain aligned with the main trend, resulting in an improved linear correlation at this collision energy. See also [48].
- [37] Lipei Du, Chun Shen, Sangyong Jeon, and Charles Gale, “Probing initial baryon stopping and equation of state with rapidity-dependent directed flow of identified particles,” *Phys. Rev. C* **108**, L041901 (2023), [arXiv:2211.16408 \[nucl-th\]](#).
- [38] Lipei Du, “Bulk medium properties of heavy-ion collisions from the beam energy scan with a multistage hydrodynamic model,” *Phys. Rev. C* **110**, 014904 (2024), [arXiv:2401.00596 \[hep-ph\]](#).
- [39] B. I. Abelev *et al.* (STAR), “Systematic Measurements of Identified Particle Spectra in pp , $d^+ + \text{Au}$ and $\text{Au} + \text{Au}$ Collisions from STAR,” *Phys. Rev. C* **79**, 034909 (2009), [arXiv:0808.2041 \[nucl-ex\]](#).
- [40] L. Adamczyk *et al.* (STAR), “Bulk Properties of the Medium Produced in Relativistic Heavy-Ion Collisions from the Beam Energy Scan Program,” *Phys. Rev. C* **96**, 044904 (2017), [arXiv:1701.07065 \[nucl-ex\]](#).
- [41] Jaroslav Adam *et al.* (STAR), “Bulk properties of the system formed in $\text{Au} + \text{Au}$ collisions at $\sqrt{s_{NN}} = 14.5$ GeV at the BNL STAR detector,” *Phys. Rev. C* **101**, 024905 (2020), [arXiv:1908.03585 \[nucl-ex\]](#).
- [42] B. B. Back *et al.* (PHOBOS), “The Significance of the fragmentation region in ultrarelativistic heavy ion collisions,” *Phys. Rev. Lett.* **91**, 052303 (2003), [arXiv:nucl-ex/0210015](#).
- [43] B. B. Back *et al.* (PHOBOS), “Charged-particle pseudorapidity distributions in $\text{Au} + \text{Au}$ collisions at $\sqrt{s_{NN}} = 62.4$ GeV,” *Phys. Rev. C* **74**, 021901 (2006), [arXiv:nucl-ex/0509034](#).
- [44] I. C. Arsene *et al.* (BRAHMS), “Kaon and Pion Production in Central $\text{Au} + \text{Au}$ Collisions at $\sqrt{s_{NN}} = 62.4$ GeV,” *Phys. Lett. B* **687**, 36–41 (2010), [arXiv:0911.2586 \[nucl-ex\]](#).
- [45] I. C. Arsene *et al.* (BRAHMS), “Nuclear stopping and rapidity loss in $\text{Au} + \text{Au}$ collisions at $\sqrt{s_{NN}} = 62.4$ GeV,” *Phys. Lett. B* **677**, 267–271 (2009), [arXiv:0901.0872 \[nucl-ex\]](#).
- [46] I. G. Bearden *et al.* (BRAHMS), “Nuclear stopping in $\text{Au} + \text{Au}$ collisions at $\sqrt{s_{NN}} = 200$ GeV,” *Phys. Rev. Lett.* **93**, 102301 (2004), [arXiv:nucl-ex/0312023](#).
- [47] I. G. Bearden *et al.* (BRAHMS), “Pseudorapidity distributions of charged particles from $\text{Au} + \text{Au}$ collisions at the maximum RHIC energy,” *Phys. Rev. Lett.* **88**, 202301 (2002), [arXiv:nucl-ex/0112001](#).
- [48] As noted in [36], the prehydrodynamic stage becomes increasingly relevant at lower collision energies due to the prolonged nuclear interpenetration process. During this stage, continuous energy deposition leads to rapidly rising temperatures, peaking once the nuclei pass through each other, accompanied by an evolution towards chemical equilibrium. Both effects suppress photon and dilepton production during this early phase, limiting its contribution to the final spectra. The modest deviation from linearity observed at 7.7 GeV in Fig. 1 may reflect the influence of this presently neglected component. Prehydrodynamic emission could affect the lower left regions of Figs. 1 and 2 and will therefore be incorporated in future work.

- [49] Chun Shen, Ulrich W. Heinz, Jean-Francois Paquet, Igor Kozlov, and Charles Gale, “Anisotropic flow of thermal photons as a quark-gluon plasma viscometer,” *Phys. Rev. C* **91**, 024908 (2015), [arXiv:1308.2111 \[nucl-th\]](#).
- [50] Mikko Laine and Aleksu Vuorinen, *Basics of Thermal Field Theory*, Vol. 925 (Springer, 2016) [arXiv:1701.01554 \[hep-ph\]](#).
- [51] Peter Brockway Arnold, Guy D. Moore, and Laurence G. Yaffe, “Photon emission from quark gluon plasma: Complete leading order results,” *JHEP* **12**, 009 (2001), [arXiv:hep-ph/0111107](#).
- [52] Hualong Gervais and Sangyong Jeon, “Photon Production from a Quark-Gluon-Plasma at Finite Baryon Chemical Potential,” *Phys. Rev. C* **86**, 034904 (2012), [arXiv:1206.6086 \[nucl-th\]](#).
- [53] M. Laine, “NLO thermal dilepton rate at non-zero momentum,” *JHEP* **11**, 120 (2013), [arXiv:1310.0164 \[hep-ph\]](#).
- [54] I. Ghisoiu and M. Laine, “Interpolation of hard and soft dilepton rates,” *JHEP* **10**, 083 (2014), [arXiv:1407.7955 \[hep-ph\]](#).
- [55] J. Cleymans, H. Oeschler, K. Redlich, and S. Wheaton, “Comparison of chemical freeze-out criteria in heavy-ion collisions,” *Phys. Rev. C* **73**, 034905 (2006), [arXiv:hep-ph/0511094](#).
- [56] L. Adamczyk *et al.* (STAR), “Dielectron Mass Spectra from Au+Au Collisions at $\sqrt{s_{NN}} = 200$ GeV,” *Phys. Rev. Lett.* **113**, 022301 (2014), [Addendum: *Phys. Rev. Lett.* **113**, 049903 (2014)], [arXiv:1312.7397 \[hep-ex\]](#).
- [57] L. Adamczyk *et al.* (STAR), “Measurements of Dielectron Production in Au+Au Collisions at $\sqrt{s_{NN}} = 200$ GeV from the STAR Experiment,” *Phys. Rev. C* **92**, 024912 (2015), [arXiv:1504.01317 \[hep-ex\]](#).
- [58] L. Adamczyk *et al.* (STAR), “Energy dependence of acceptance-corrected dielectron excess mass spectrum at mid-rapidity in Au+Au collisions at $\sqrt{s_{NN}} = 19.6$ and 200 GeV,” *Phys. Lett. B* **750**, 64–71 (2015), [arXiv:1501.05341 \[hep-ex\]](#).
- [59] M. I. Abdulhamid *et al.* (STAR), “Measurements of dielectron production in Au+Au collisions at $\sqrt{s_{NN}}=27$, 39, and 62.4 GeV from the STAR experiment,” *Phys. Rev. C* **107**, L061901 (2023).
- [60] A. Adare *et al.* (PHENIX), “Enhanced production of direct photons in Au+Au collisions at $\sqrt{s_{NN}} = 200$ GeV and implications for the initial temperature,” *Phys. Rev. Lett.* **104**, 132301 (2010), [arXiv:0804.4168 \[nucl-ex\]](#).
- [61] A. Adare *et al.* (PHENIX), “Beam Energy and Centrality Dependence of Direct-Photon Emission from Ultrarelativistic Heavy-Ion Collisions,” *Phys. Rev. Lett.* **123**, 022301 (2019), [arXiv:1805.04084 \[hep-ex\]](#).
- [62] N. J. Abdulameer *et al.* (PHENIX), “Nonprompt direct-photon production in Au+Au collisions at $\sqrt{s_{NN}}=200$ GeV,” *Phys. Rev. C* **109**, 044912 (2024), [arXiv:2203.17187 \[nucl-ex\]](#).
- [63] Peter Brockway Arnold, Guy D. Moore, and Laurence G. Yaffe, “Photon emission from quark gluon plasma: Complete leading order results,” *JHEP* **12**, 009 (2001), [arXiv:hep-ph/0111107](#).
- [64] To eliminate transverse flow effects we modify the four-velocity u^μ of each fluid cell by setting the spatial components $u^x = u^y = 0$ and adjusting u^z to maintain $u^\mu u_\mu = 1$. This modified velocity is then used to compute the photon spectra.
- [65] G. Jackson and M. Laine, “Testing thermal photon and dilepton rates,” *JHEP* **11**, 144 (2019), [arXiv:1910.09567 \[hep-ph\]](#).
- [66] Peter Brockway Arnold, Guy D. Moore, and Laurence G. Yaffe, “Photon emission from ultrarelativistic plasmas,” *JHEP* **11**, 057 (2001), [arXiv:hep-ph/0109064](#).
- [67] Jaroslav Adam *et al.* (ALICE), “Anisotropic flow of charged particles in Pb-Pb collisions at $\sqrt{s_{NN}} = 5.02$ TeV,” *Phys. Rev. Lett.* **116**, 132302 (2016), [arXiv:1602.01119 \[nucl-ex\]](#).
- [68] L. Adamczyk *et al.* (STAR), “Harmonic decomposition of three-particle azimuthal correlations at energies available at the BNL Relativistic Heavy Ion Collider,” *Phys. Rev. C* **98**, 034918 (2018), [arXiv:1701.06496 \[nucl-ex\]](#).
- [69] Ekkard Schnedermann, Josef Sollfrank, and Ulrich W. Heinz, “Thermal phenomenology of hadrons from 200-A/GeV S+S collisions,” *Phys. Rev. C* **48**, 2462–2475 (1993), [arXiv:nucl-th/9307020](#).
- [70] Edward V. Shuryak and L. Xiong, “Dilepton and photon production in the ‘hot glue’ scenario,” *Phys. Rev. Lett.* **70**, 2241–2244 (1993), [arXiv:hep-ph/9301218](#).
- [71] Hannah Petersen, Jan Steinheimer, Gerhard Burau, Marcus Bleicher, and Horst Stöcker, “A Fully Integrated Transport Approach to Heavy Ion Reactions with an Intermediate Hydrodynamic Stage,” *Phys. Rev. C* **78**, 044901 (2008), [arXiv:0806.1695 \[nucl-th\]](#).
- [72] Sangwook Ryu, Jean-François Paquet, Chun Shen, Gabriel Denicol, Björn Schenke, Sangyong Jeon, and Charles Gale, “Effects of bulk viscosity and hadronic rescattering in heavy ion collisions at energies available at the BNL Relativistic Heavy Ion Collider and at the CERN Large Hadron Collider,” *Phys. Rev. C* **97**, 034910 (2018), [arXiv:1704.04216 \[nucl-th\]](#).
- [73] L.D. acknowledges the use of Grammarly and AI-based writing assistants for grammar refinement and clarity enhancement during the final editing of the manuscript. All revisions were carefully reviewed to ensure that the intended meaning and scientific content remained unchanged.
- [74] “Ohio Supercomputer Center,” (1987).
- [75] Björn Schenke, Chun Shen, and Derek Teaney, “Transverse momentum fluctuations and their correlation with elliptic flow in nuclear collision,” *Phys. Rev. C* **102**, 034905 (2020), [arXiv:2004.00690 \[nucl-th\]](#).
- [76] Chun Shen, Björn Schenke, and Wenbin Zhao, “Viscosities of the Baryon-Rich Quark-Gluon Plasma from Beam Energy Scan Data,” *Phys. Rev. Lett.* **132**, 072301 (2024), [arXiv:2310.10787 \[nucl-th\]](#).

Correlation between dilepton and photon temperatures

In the main text, we leverage the empirical observation that the temperature extracted from the dilepton invariant mass spectrum ($T_{\ell\bar{\ell}}$) provides a reliable proxy for the unobservable photon temperature in the absence of transverse flow ($T_{\gamma 0}$), owing to their strong linear correlation shown in Fig. 1. This correlation enables an experimentally feasible determination of the effective radial flow, using the measurable photon temperature T_{γ} and a model-calibrated estimate of $T_{\gamma 0}$ derived from $T_{\ell\bar{\ell}}$.

We find that $T_{\ell\bar{\ell}}$ increasingly exceeds $T_{\gamma 0}$ at higher beam energies, which we interpret as a natural consequence of the longer fireball lifetime. Over time, the roughly constant offset $\Delta T = T_{\ell\bar{\ell}} - T_{\gamma 0}$ accumulates, leading to a larger deviation in the temperatures derived from time-integrated spectra. This constant offset in time was previously observed in [L. Du, Phys. Lett. B 861 (2025) 139270], where time-resolved analyses at $\sqrt{s_{\text{NN}}} = 7.7$ and 14.5 GeV revealed that $T_{\ell\bar{\ell}}$ and $T_{\gamma 0}$, extracted at each time step, evolve in parallel with an approximately constant separation ΔT .

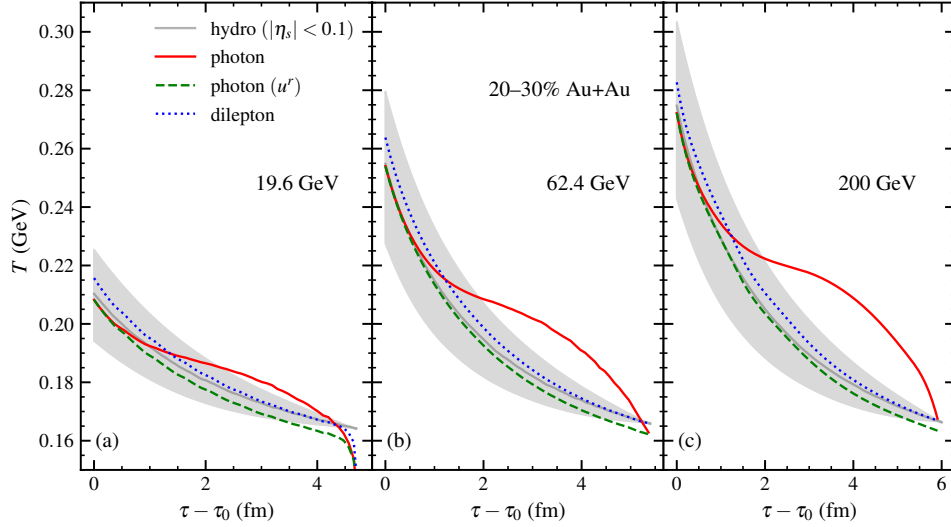


Figure 4. Time evolution of effective temperatures extracted from photon and dilepton spectra at $\sqrt{s_{\text{NN}}} = 19.6, 62.4$, and 200 GeV (panels (a)–(c)). Each panel shows the photon temperature with (T_{γ} , red solid) and without transverse flow ($T_{\gamma 0}$, green dashed), the dilepton-inferred temperature ($T_{\ell\bar{\ell}}$, blue dotted), and the hydrodynamic average temperature (gray curve) with its variation (gray band)^a in 20–30% Au+Au collisions at midrapidity. At each energy, $T_{\gamma 0}$ and $T_{\ell\bar{\ell}}$ track each other closely throughout the evolution, separated by an approximately constant offset ΔT .

^a Same as in the main text, an averaged quantity $\langle O \rangle$ is defined as a weighted average over fluid cells with weight $e\gamma$, i.e., $\langle O \rangle = \sum(O \cdot e\gamma) / \sum(e\gamma)$. The gray curve shows this average, while the gray band represents the standard deviation, reflecting the variation among contributing fluid cells. The average radial flow shown in Fig. 5 is defined in the same way.

To test the generality of this behavior across a broader range of beam energies and centralities, we extend the time-differential analysis to nine energies between $\sqrt{s_{\text{NN}}} = 7.7$ and 200 GeV. Figure 4 shows the time evolution of $T_{\ell\bar{\ell}}$ and $T_{\gamma 0}$ at midrapidity in 20–30% Au+Au collisions for three representative energies: $\sqrt{s_{\text{NN}}} = 19.6, 62.4$, and 200 GeV. In all cases, $T_{\ell\bar{\ell}}$ consistently lies above $T_{\gamma 0}$ throughout the hydrodynamic evolution, with the two curves maintaining a nearly constant offset of a few MeV. Although the overall temperature scale rises with collision energy, the offset ΔT remains approximately constant during the evolution.

Figure 5 evaluates the impact of this approximation on flow extraction. The effective radial flow is computed using the blue-shift relation between T_{γ} and either (i) the true $T_{\gamma 0}$ obtained from simulations, or (ii) an adjusted $T_{\ell\bar{\ell}}$ serving as a proxy for $T_{\gamma 0}$ via $T_{\gamma 0} \approx T_{\ell\bar{\ell}} - \Delta T$. The results demonstrate that the flow extracted using the “photon+dilepton” method closely reproduces the reference result obtained with both photon temperatures. The agreement holds across energies and persists throughout the evolution, with small deviations appearing only at early and late times.

Across all nine beam energies and eight centralities, we find that a constant offset $\Delta T = 4.5$ MeV reproduces $T_{\gamma 0}$ from $T_{\ell\bar{\ell}}$ for $\sqrt{s_{\text{NN}}} > 7.7$ GeV, while a slightly smaller value $\Delta T = 4$ MeV suffices at $\sqrt{s_{\text{NN}}} = 7.7$ GeV. These findings confirm the robustness of the $T_{\ell\bar{\ell}}-T_{\gamma 0}$ correlation and its near-constant offset in time. While this time-resolved offset is not directly employed in the main analysis, it provides crucial insight into why $T_{\ell\bar{\ell}}$ increasingly exceeds $T_{\gamma 0}$ in integrated spectra at higher collision energies.

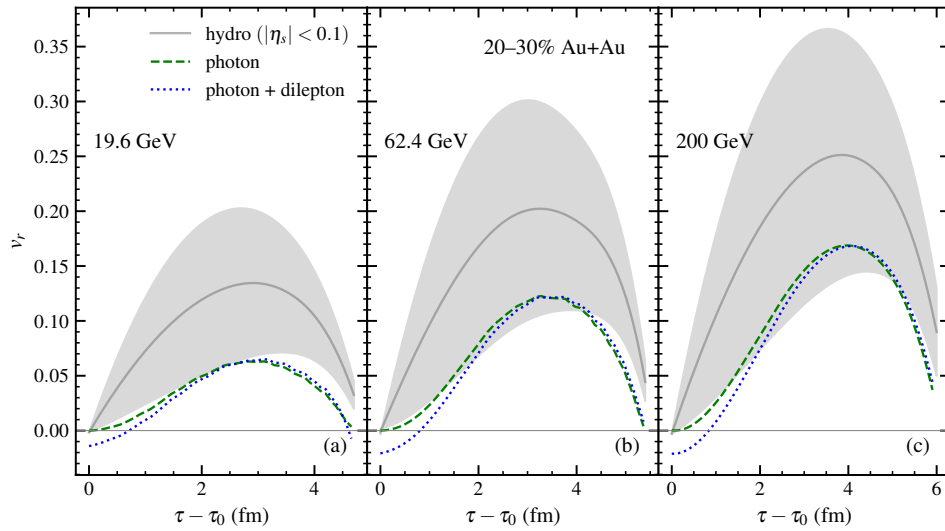


Figure 5. Comparison of effective radial flow extracted using true and proxy baselines for the no-flow photon temperature. For each beam energy shown in Fig. 4, the radial flow v_r is computed from the blue-shift relation using the measured T_γ and either the true $T_{\gamma 0}$ (green dashed) or the proxy estimate $T_{\ell\bar{\ell}} - \Delta T$ (blue dotted, denoted as “photon+dilepton”). The gray curve shows the hydrodynamic average radial flow, and the gray band indicates its standard deviation, reflecting variations among fluid cells weighted as described in footnote a.

Table I. Temperature observables at midrapidity across beam energies and centralities.

$\sqrt{s_{NN}}$ (GeV)	T (MeV)	Centrality							
		0–10%	10–20%	20–30%	30–40%	40–50%	50–60%	60–70%	70–80%
7.7	$T_{\ell\bar{\ell}}$	204 ± 4	202 ± 4	200 ± 4	197 ± 4	193 ± 4	189 ± 4	183 ± 3	156 ± 1
	$T_{\gamma 0}$	172 ± 0	171 ± 0	169 ± 0	167 ± 0	165 ± 0	161 ± 0	156 ± 0	133 ± 1
	T_γ	174 ± 0	173 ± 0	171 ± 0	169 ± 0	166 ± 0	162 ± 0	156 ± 0	133 ± 1
14.5	$T_{\ell\bar{\ell}}$	227 ± 4	225 ± 4	222 ± 4	218 ± 4	213 ± 4	208 ± 4	202 ± 4	196 ± 4
	$T_{\gamma 0}$	187 ± 1	185 ± 1	183 ± 1	181 ± 1	178 ± 1	175 ± 0	171 ± 0	167 ± 0
	T_γ	190 ± 1	189 ± 1	187 ± 1	184 ± 1	181 ± 1	177 ± 1	172 ± 0	168 ± 0
19.6	$T_{\ell\bar{\ell}}$	237 ± 3	235 ± 4	231 ± 4	227 ± 4	222 ± 4	215 ± 4	208 ± 4	202 ± 4
	$T_{\gamma 0}$	193 ± 1	191 ± 1	189 ± 1	187 ± 1	183 ± 1	180 ± 1	175 ± 0	171 ± 0
	T_γ	197 ± 1	195 ± 1	194 ± 1	191 ± 1	187 ± 1	183 ± 1	177 ± 1	172 ± 0
27	$T_{\ell\bar{\ell}}$	252 ± 3	249 ± 3	245 ± 3	240 ± 3	234 ± 4	226 ± 4	218 ± 4	210 ± 4
	$T_{\gamma 0}$	201 ± 1	199 ± 1	197 ± 1	194 ± 1	191 ± 1	186 ± 1	181 ± 1	177 ± 0
	T_γ	206 ± 1	205 ± 1	203 ± 1	200 ± 1	196 ± 1	191 ± 1	184 ± 1	179 ± 1
39	$T_{\ell\bar{\ell}}$	268 ± 2	265 ± 3	260 ± 3	254 ± 3	247 ± 3	238 ± 3	228 ± 4	219 ± 4
	$T_{\gamma 0}$	209 ± 2	208 ± 2	205 ± 2	202 ± 1	198 ± 1	193 ± 1	187 ± 1	182 ± 1
	T_γ	215 ± 2	214 ± 2	212 ± 2	209 ± 1	204 ± 1	199 ± 1	192 ± 1	185 ± 1
54.4	$T_{\ell\bar{\ell}}$	278 ± 2	275 ± 2	270 ± 2	263 ± 3	255 ± 3	246 ± 3	234 ± 4	224 ± 4
	$T_{\gamma 0}$	215 ± 2	213 ± 2	210 ± 2	207 ± 2	203 ± 2	197 ± 1	191 ± 1	185 ± 1
	T_γ	221 ± 2	220 ± 2	217 ± 2	214 ± 2	210 ± 1	204 ± 1	196 ± 1	189 ± 1
62.4	$T_{\ell\bar{\ell}}$	281 ± 2	278 ± 2	273 ± 2	266 ± 3	258 ± 3	248 ± 3	236 ± 4	225 ± 4
	$T_{\gamma 0}$	216 ± 2	215 ± 2	212 ± 2	209 ± 2	204 ± 2	199 ± 1	192 ± 1	186 ± 1
	T_γ	223 ± 2	222 ± 2	219 ± 2	216 ± 2	211 ± 2	205 ± 1	198 ± 1	190 ± 1
130	$T_{\ell\bar{\ell}}$	293 ± 2	289 ± 2	283 ± 2	276 ± 2	267 ± 3	256 ± 3	243 ± 3	230 ± 4
	$T_{\gamma 0}$	223 ± 3	221 ± 2	218 ± 2	214 ± 2	209 ± 2	203 ± 2	196 ± 1	189 ± 1
	T_γ	230 ± 2	229 ± 2	226 ± 2	223 ± 2	218 ± 2	211 ± 1	202 ± 1	194 ± 1
200	$T_{\ell\bar{\ell}}$	305 ± 1	301 ± 1	295 ± 2	287 ± 2	278 ± 2	265 ± 3	251 ± 3	237 ± 3
	$T_{\gamma 0}$	229 ± 3	227 ± 3	224 ± 3	220 ± 2	215 ± 2	208 ± 2	200 ± 1	193 ± 1
	T_γ	237 ± 2	236 ± 2	233 ± 2	230 ± 2	224 ± 2	217 ± 2	208 ± 1	199 ± 1

Table II. Radial flow observables at midrapidity across beam energies and centralities.

$\sqrt{s_{NN}}$ (GeV)	v_r (c)	Centrality							
		0–10%	10–20%	20–30%	30–40%	40–50%	50–60%	60–70%	70–80%
7.7	v_r^{eff}	0.010 ± 0.002	0.010 ± 0.002	0.010 ± 0.002	0.008 ± 0.002	0.006 ± 0.002	0.003 ± 0.003	0.001 ± 0.004	0.000 ± 0.008
	v_r^{prefrz}	0.045 ± 0.038	0.044 ± 0.038	0.042 ± 0.035	0.039 ± 0.031	0.032 ± 0.025	0.022 ± 0.017	0.011 ± 0.008	0.019 ± 0.012
	v_r^{frz}	0.208 ± 0.090	0.205 ± 0.090	0.193 ± 0.090	0.174 ± 0.087	0.148 ± 0.081	0.116 ± 0.071	0.079 ± 0.056	0.044 ± 0.039
14.5	v_r^{eff}	0.017 ± 0.006	0.018 ± 0.006	0.019 ± 0.006	0.018 ± 0.005	0.016 ± 0.005	0.012 ± 0.004	0.007 ± 0.003	0.003 ± 0.003
	v_r^{prefrz}	0.062 ± 0.058	0.064 ± 0.058	0.064 ± 0.057	0.062 ± 0.053	0.057 ± 0.047	0.048 ± 0.039	0.036 ± 0.029	0.024 ± 0.017
	v_r^{frz}	0.278 ± 0.113	0.273 ± 0.114	0.261 ± 0.115	0.242 ± 0.114	0.216 ± 0.111	0.182 ± 0.103	0.142 ± 0.091	0.102 ± 0.076
19.6	v_r^{eff}	0.021 ± 0.007	0.022 ± 0.007	0.023 ± 0.007	0.022 ± 0.006	0.020 ± 0.006	0.016 ± 0.005	0.011 ± 0.004	0.007 ± 0.003
	v_r^{prefrz}	0.070 ± 0.067	0.072 ± 0.067	0.073 ± 0.066	0.072 ± 0.062	0.067 ± 0.057	0.059 ± 0.048	0.047 ± 0.038	0.036 ± 0.028
	v_r^{frz}	0.306 ± 0.121	0.301 ± 0.124	0.288 ± 0.125	0.269 ± 0.125	0.243 ± 0.121	0.208 ± 0.115	0.168 ± 0.104	0.125 ± 0.090
27	v_r^{eff}	0.024 ± 0.010	0.026 ± 0.009	0.027 ± 0.009	0.027 ± 0.008	0.026 ± 0.007	0.023 ± 0.006	0.018 ± 0.005	0.012 ± 0.004
	v_r^{prefrz}	0.079 ± 0.078	0.082 ± 0.079	0.083 ± 0.077	0.083 ± 0.074	0.080 ± 0.069	0.072 ± 0.061	0.062 ± 0.050	0.050 ± 0.039
	v_r^{frz}	0.338 ± 0.131	0.332 ± 0.134	0.320 ± 0.136	0.301 ± 0.136	0.274 ± 0.134	0.240 ± 0.129	0.198 ± 0.118	0.152 ± 0.106
39	v_r^{eff}	0.026 ± 0.012	0.028 ± 0.011	0.030 ± 0.011	0.031 ± 0.010	0.031 ± 0.009	0.028 ± 0.008	0.023 ± 0.006	0.018 ± 0.005
	v_r^{prefrz}	0.085 ± 0.087	0.089 ± 0.088	0.091 ± 0.087	0.092 ± 0.084	0.089 ± 0.079	0.083 ± 0.071	0.073 ± 0.061	0.064 ± 0.050
	v_r^{frz}	0.365 ± 0.139	0.359 ± 0.143	0.347 ± 0.145	0.328 ± 0.146	0.302 ± 0.145	0.267 ± 0.140	0.224 ± 0.131	0.177 ± 0.120
54.4	v_r^{eff}	0.028 ± 0.014	0.031 ± 0.013	0.032 ± 0.012	0.034 ± 0.011	0.033 ± 0.010	0.031 ± 0.009	0.027 ± 0.007	0.022 ± 0.006
	v_r^{prefrz}	0.090 ± 0.094	0.094 ± 0.095	0.097 ± 0.094	0.098 ± 0.091	0.096 ± 0.086	0.090 ± 0.078	0.080 ± 0.067	0.070 ± 0.057
	v_r^{frz}	0.385 ± 0.144	0.379 ± 0.148	0.367 ± 0.150	0.347 ± 0.152	0.321 ± 0.151	0.286 ± 0.147	0.239 ± 0.139	0.192 ± 0.127
62.4	v_r^{eff}	0.029 ± 0.014	0.032 ± 0.013	0.034 ± 0.013	0.035 ± 0.012	0.035 ± 0.011	0.033 ± 0.009	0.028 ± 0.007	0.023 ± 0.006
	v_r^{prefrz}	0.093 ± 0.096	0.097 ± 0.098	0.100 ± 0.097	0.101 ± 0.094	0.099 ± 0.089	0.093 ± 0.081	0.083 ± 0.070	0.073 ± 0.059
	v_r^{frz}	0.393 ± 0.146	0.387 ± 0.150	0.374 ± 0.153	0.354 ± 0.154	0.328 ± 0.153	0.292 ± 0.150	0.247 ± 0.141	0.198 ± 0.130
130	v_r^{eff}	0.033 ± 0.015	0.036 ± 0.015	0.038 ± 0.014	0.039 ± 0.013	0.039 ± 0.012	0.037 ± 0.010	0.033 ± 0.008	0.027 ± 0.006
	v_r^{prefrz}	0.102 ± 0.106	0.106 ± 0.107	0.109 ± 0.106	0.110 ± 0.103	0.108 ± 0.097	0.102 ± 0.089	0.091 ± 0.078	0.078 ± 0.066
	v_r^{frz}	0.422 ± 0.151	0.415 ± 0.156	0.402 ± 0.159	0.381 ± 0.161	0.352 ± 0.160	0.315 ± 0.157	0.269 ± 0.149	0.215 ± 0.137
200	v_r^{eff}	0.036 ± 0.017	0.039 ± 0.016	0.041 ± 0.015	0.043 ± 0.014	0.043 ± 0.013	0.042 ± 0.012	0.037 ± 0.010	0.032 ± 0.008
	v_r^{prefrz}	0.108 ± 0.116	0.113 ± 0.117	0.116 ± 0.116	0.117 ± 0.113	0.116 ± 0.107	0.110 ± 0.099	0.100 ± 0.087	0.088 ± 0.073
	v_r^{frz}	0.449 ± 0.156	0.441 ± 0.161	0.428 ± 0.164	0.407 ± 0.166	0.379 ± 0.168	0.339 ± 0.165	0.291 ± 0.158	0.236 ± 0.147